International Forum on Aeroelasticity and Structural Dynamics
IFASD 2017
25-28 June 2017 Como, Italy

TRANSONIC AEROELASTICITY USING THE 2.5D NON-LINEAR VORTEX-LATTICE METHOD

A.Grozdanov[1] **and E.Laurendeau**[2]

[1]M.Sc.A, Department of Mechanical Engineering
Polytechnique Montreal
Chemin de Polytechnique, 2500 Montreal H3T 1J4 Canada
atanas.grozdanov@polymtl.ca

[2]Professor, Department of Mechanical Engineering
Polytechnique Montreal
Chemin de Polytechnique, 2500 Montreal H3T 1J4 Canada
eric.laurendeau@polymtl.ca

Keywords: Transonic, computational fluid dynamics, aeroelasticity, optimization, hirenasd, CRM

Abstract: Three-dimensional aeroelastic effects in the transonic flight regime can be analyzed by combining high-fidelity 3D CFD solutions with structural finite element models containing a large number of degrees of freedom. This combination is computationally expensive and is impractical in the preliminary design phase. Here, a non-linear vortex-lattice method that couples 2.5D transonic CFD solutions is examined. As such, it provides adequate precision for the study of three-dimensional aeroelastic effects at the computational cost of a VLM solution. This paper presents the combination of this method with a finite element beam model and demonstrates that this inexpensive method is suitable for the prediction of wing behavior in the transonic regime.

1 INTRODUCTION

The steady and unsteady vortex-lattice method coupled with a beam model has previously been investigated, and its suitability for subsonic aeroelasticity demonstrated [1]. In the case of transonic flight, however, it is inadequate and three-dimensional CFD methods coupled with large finite-element models have been used in order to capture the variation in the aerodynamic coefficients that is due to the appearance of supersonic flow regions [2] [3].

The addition of viscous coupling to the vortex-lattice method to form the 2.5D non-linear vortex-lattice method (2.5D NL-VLM) has been demonstrated to extend its range of applicability to transonic flight conditions [4] [5]. Furthermore, through interpolation along the span, it can provide a three-dimensional flow field with a more accurate force distribution to the structure than the potential flow alone can. This further encourages the use of a segregated coupling algorithm, as it delivers the possibility of going beyond beam models to fully exploit the capabilities of medium-fidelity modeling.

2 OBJECTIVES

The objective is to investigate the capability of the 2.5D NL-VLM method for static aeroelasticity in the subsonic and transonic flight regime, for both attached and separated flows. In particular, the 2.5D NL-VLM method is augmented with a finite element beam model via efficient coupling strategies. The applicability of this new medium fidelity approach is investigated in the context of preliminary design of aircraft.

3 WORK DESCRIPTION

This framework's inviscid aeroelastic coupling is validated by finding the static trim characteristics of the High-Altitude Long-Endurance (HALE) aircraft studied by Murua et al.[2012].

The addition of the viscous coupling is assessed by replicating the wind-tunnel correction performed by Keye for the Common Research Model [2]. The capability of the method to predict the transonic flow-field of transonic wings is further investigated for the HIRENASD wing [6] [7] [3].

4 METHODOLOGY

Because of the relevance of the method for preliminary and perhaps conceptual design, a segregated approach is chosen to facilitate the integration of the method into an industrial context, where monolithic integration is unlikely. [8] [9].

4.1 Aerodynamics

The 2.5D NL-VLM aerodynamic model combines the traditional vortex-lattice method [10] with a 2D CFD solver, both in steady and unsteady formulations. The extension of the method into the transonic regime is provided by a viscous coupling as described by Gallay et al.[2015], having both loose and strong viscous coupling capabilities. In particular, the use of the infinite swept wing (2.5D) assumption into the 2D RANS solver enables the capture of stagnation lines, oblique shock waves and cross-flow separation. [11]

The viscous database is generated with in-house codes NSGRID [12] and NSCODE [13] [14], the former provides the RANS meshes and the later computes the 2.5D RANS solution using standard algorithms.

For the CRM wing, the viscous database computations were done at a Mach number of 0.85, Reynolds number of 5e6 and a Spalart-Allmaras turbulence model. For the Hirenasd wing, the computations were done at a Mach Number of 0.70, with a Reynolds number of 7e6 and a Spalart-Allmaras turbulence model. For both wings, the quarter-chord sweep at each respective station was used for the infinite swept wing computation, 2D RANS computations having been done on 9 individual spanwise stations for the CRM wing and 10 individual spanwise stations for the Hirenasd Wing.

4.2 Structure

An in-house, dedicated object-oriented finite-element solver (OFEM) is used that provides combinations of linear, geometrically nonlinear, steady and unsteady beams for structural modeling [15]. It is assumed that the structure's dominant modes are adequately represented by two-noded beams having bending, torsion and traction degree of freedoms [16]. Due to the low

number of elements that this approach requires, the wing deformations are obtained at a similar computational cost as the loads provided by the 2.5D NL-VLM method.

To ensure that the dimensions of the aerodynamic surfaces are not modified with increasing deflection, all finite element computations are geometrically nonlinear. Multiple loading steps are applied onto the modified Newton method to accurately converge on the tip displacements and prevent unphysical elongation of the beams, which would artificially increase the area of the lifting surface and thus have an undesirable effect on the loads.

Furthermore, the beams are positioned at the elastic axis of the wings with appropriate section properties [17] which are computed by taking spanwise cuts of the wing's structure perpendicular to the elastic axis. The polygons that are thus produced are fed into the following equations to obtain the area and first moments of inertia, with material being added counter-clockwise and voids being added clockwise to produce the correct signs

$$A = \frac{1}{2} \sum_{i=0}^{npts-1} (y_i + y_{i+1})(z_{i+1} - z_i) \tag{1}$$

$$Q_y = \frac{1}{2} \sum_{i=0}^{npts-1} (y_i - y_{i+1})(z_i z_{i+1} + \frac{1}{3}(z_i - z_{i+1})^2) \tag{2}$$

$$Q_z = \frac{1}{2} \sum_{i=0}^{npts-1} (z_{i+1} - z_i)(y_i y_{i+1} + \frac{1}{3}(y_i - y_{i+1})^2) \tag{3}$$

The first moments and the area are used to obtain the position of the section's centroid, which is thereafter the origin from which the second moments of inertia are computed, and serves as the position of the beam's elastic axis at the corresponding spanwise station.

$$y_{centroid} = \frac{Q_z}{A} \tag{4}$$

$$z_{centroid} = \frac{Q_y}{A} \tag{5}$$

$$I_{zz} = \frac{1}{12} \sum_{i=0}^{npts-1} (y_{i+1}^2 + y_{i+1} y_i + y_i^2)(y_i z_{i+1} - y_{i+1} z_i) \tag{6}$$

$$I_{yy} = \frac{1}{12} \sum_{i=0}^{npts-1} (z_{i+1}^2 + z_{i+1} z_i + z_i^2)(y_i z_{i+1} - y_{i+1} z_i) \tag{7}$$

This procedure automates the computation of section properties at as many span-stations as is desired and is therefore used to progressively increase the number of beam elements until the deformations have been converged upon.

In the case of the common research model wind tunnel model (CRM-WT), it was chosen to neglect cable routes, as they were positioned near the neutral axis and would have a small effect on the section properties. However, in the case of the Hirenasd wing, the four cable routes were included in the computation, as these are large and their absence would significantly overestimate the stiffness of the wing.

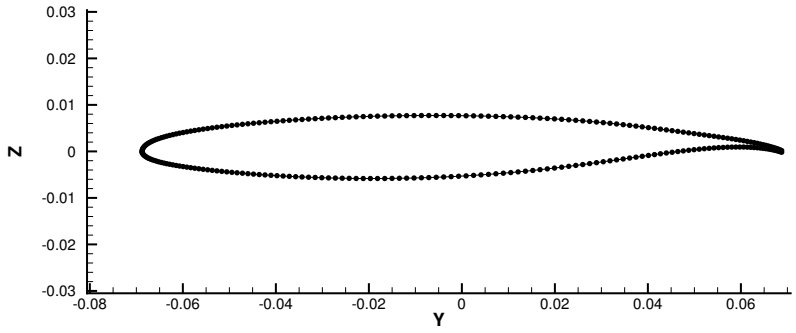

Figure 1: CRM-WT wing, beam section at $\eta = 0.53$ perpendicular to the elastic axis

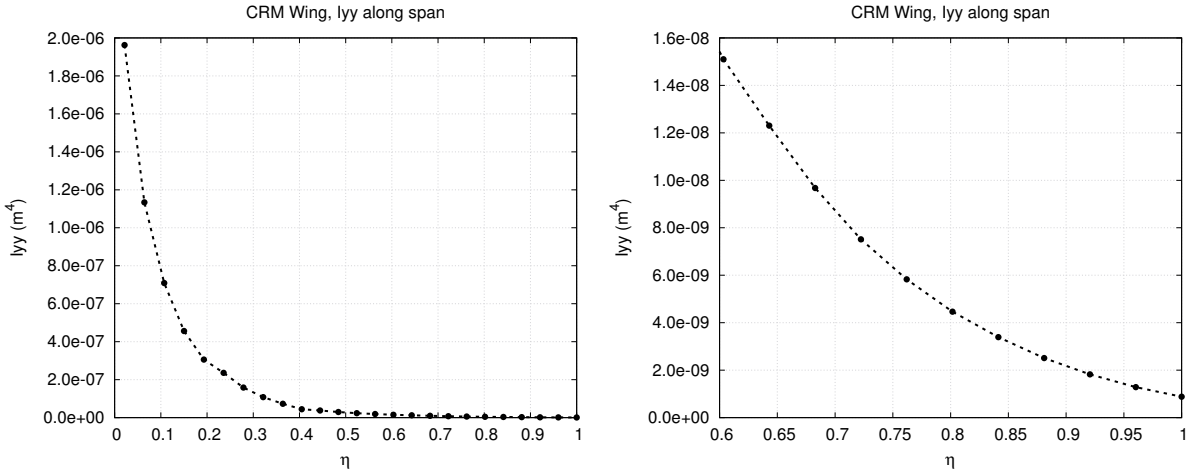

Figure 2: CRM-WT wing, I_{yy} of beam elements along the span (left) and nearing the tip (right)

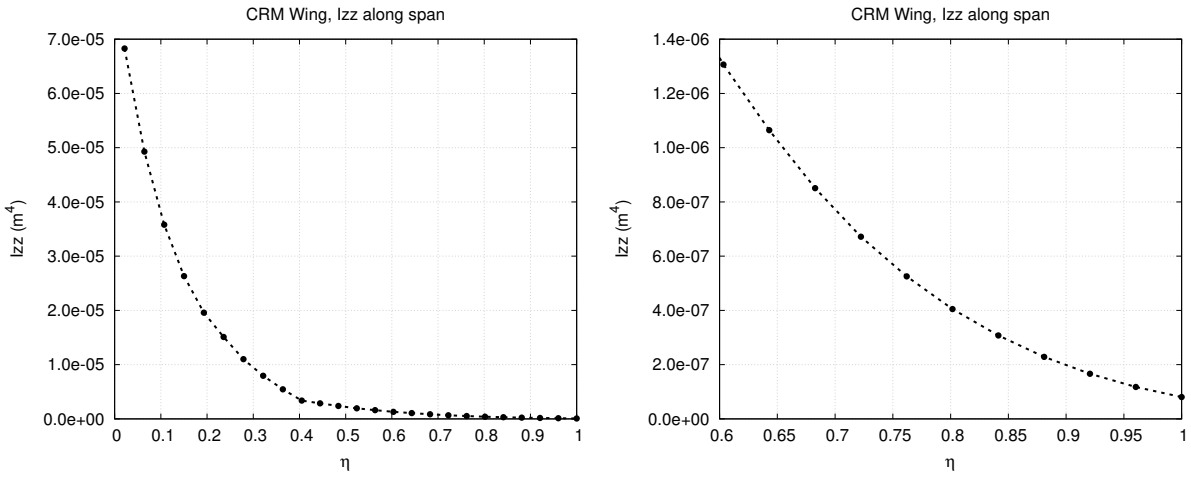

Figure 3: CRM-WT wing, I_{zz} of beam elements along the span (left) and nearing the tip (right)

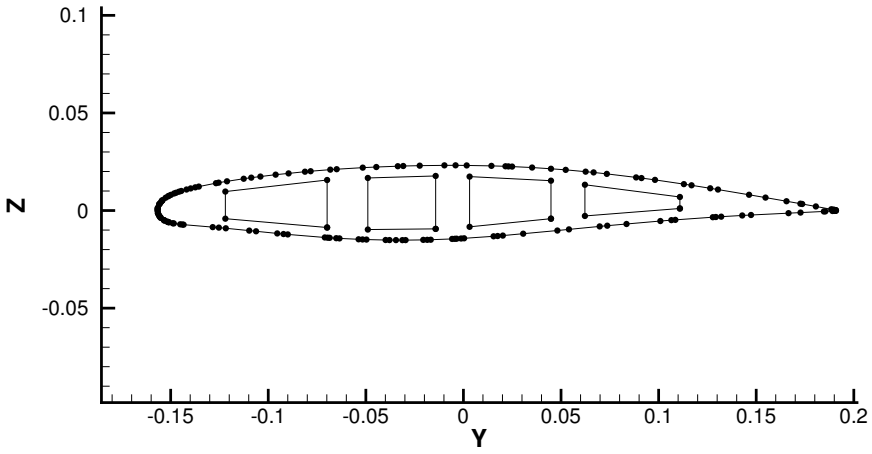

Figure 4: Hirenasd wing, beam section at $\eta = 0.41$ perpendicular to the elastic axis

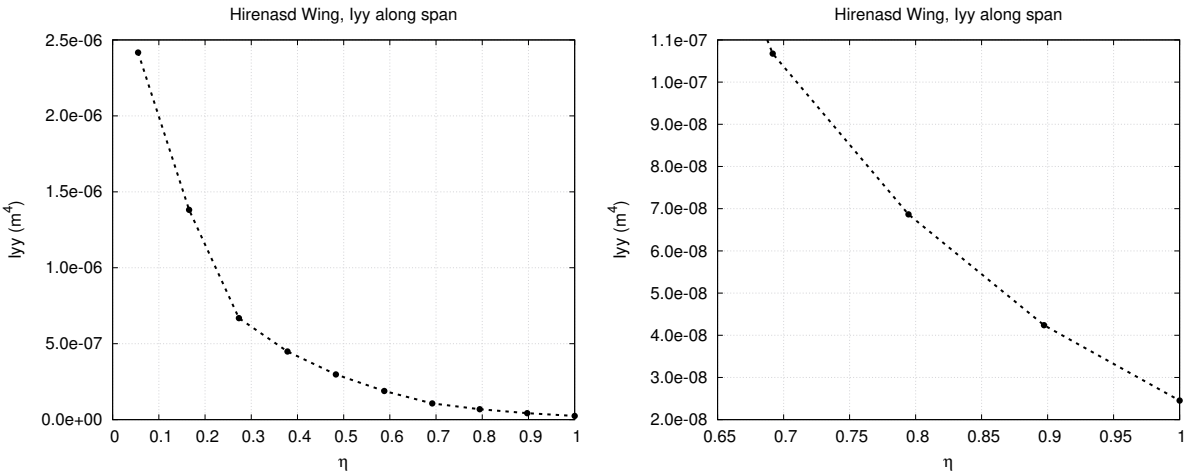

Figure 5: Hirenasd wing, I_{yy} of beam elements along the span (left) and nearing the tip (right)

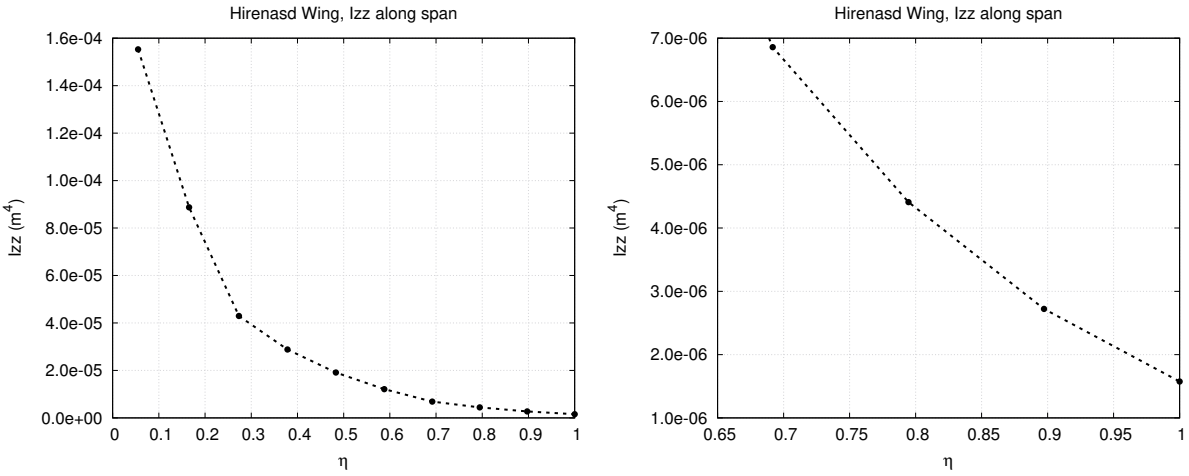

Figure 6: Hirenasd wing, I_{zz} of beam elements along the span (left) and nearing the tip (right)

4.3 Coupling

The staggered methodology requires that the individual models converge to a solution and that the boundary conditions they share converge as well. This is achieved by inter-iterations at a given time step, the forces being provided by the aerodynamic model, while the displacements and velocities are provided by the structure's finite element model. [16] This procedure is interrupted when either the relative error on the lift coefficient or the relative error on the potential energy has met a predetermined tolerance criterion.

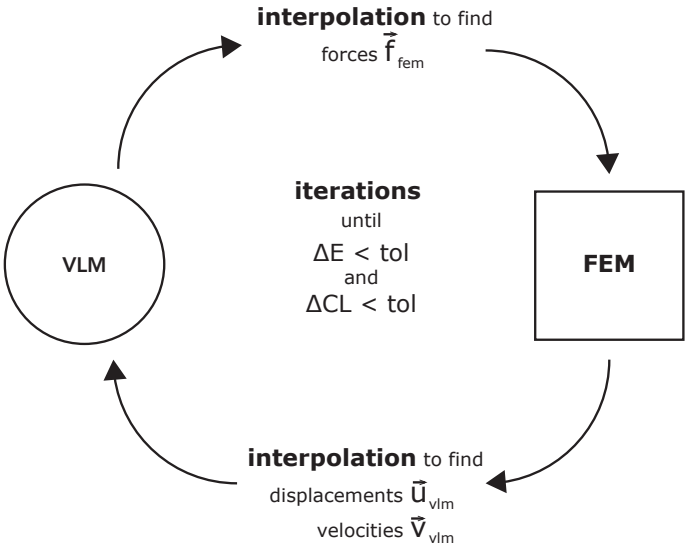

Figure 7: Segregated aeroelastic coupling procedure

With the addition of viscous coupling, there are two coupling procedures that alternate, the viscous coupling and the aeroelastic coupling, each iterating until the tolerance that was specified is met.

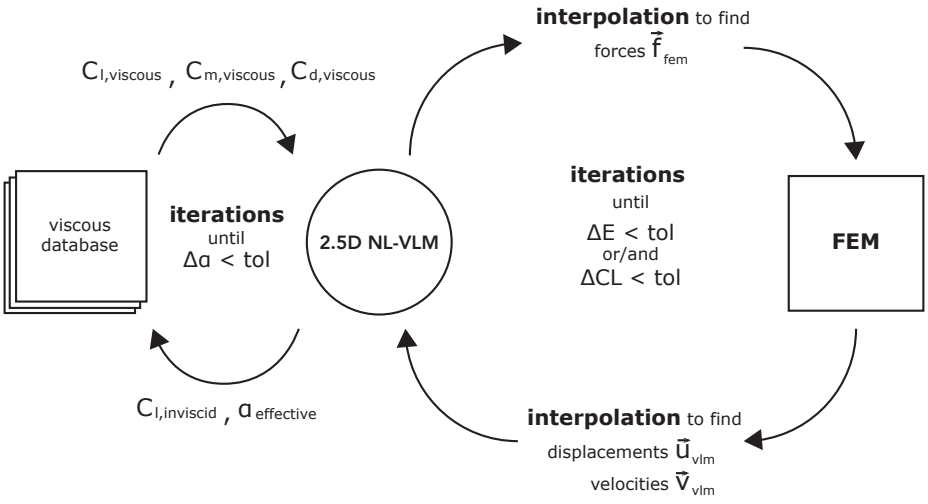

Figure 8: Segregated aeroelastic with viscous coupling procedure

This segregated coupling procedure requires two interpolation matrices to transfer loads and deformations, the first matrix H_1 assigns to each FEM node an interpolation weight for the aerodynamic forces and the second matrix H_2 assigns to every point in the VLM mesh an interpolation weight for the displacements and rotations. The rotations further have to be transformed into displacements at the VLM mesh points [16].

In the present paper, the consistent method proposed by Farhat et al.[1998] is used to compute interpolation weights by projecting either the origin of the aerodynamic loads or the destination of the displacements onto the FEM beams and using the FEM element's own interpolation functions to generate the aforementioned weights [18] [19] [20].

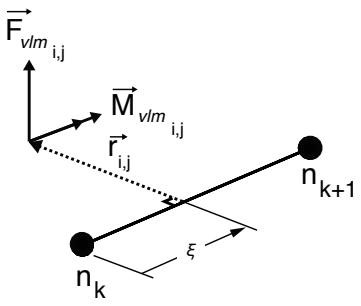

Figure 9: Projection onto nearest beam element

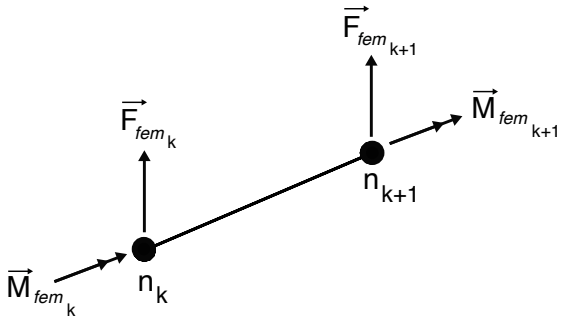

Figure 10: Loads applied onto the finite element model

For the two-noded beams used in the present paper, this equates to distributing the force and moment onto the two neighboring nodes based on the parametric fraction ξ that corresponds to the orthogonal projection of the load origin onto the beam

To couple the FEM beam model with a linear VLM, the forces from the individual vortex-rings are transfered to the FEM nodes using the interpolation weights, remembering that the vortex-ring lift forces' points of origin are between the frontal nodes of the vortex-rings [16].

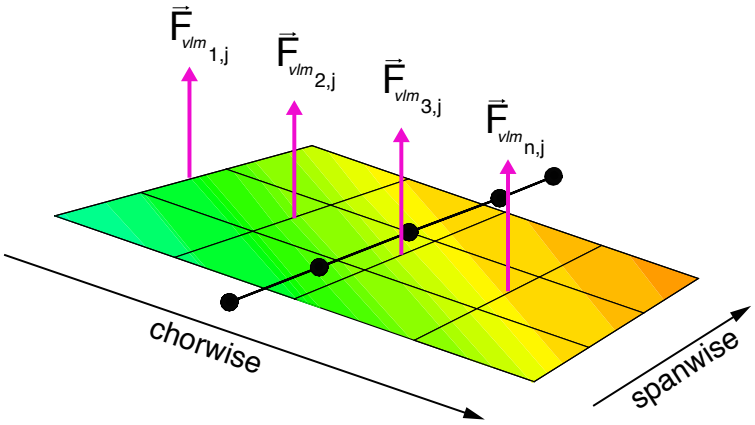

Figure 11: Forces to be applied onto the FEM for each column of vortex rings

To couple the FEM beam model with the 2.5D NL-VLM, the panel forces are disregarded and the normal and tangential aerodynamic forces from the RANS solution are instead expressed as vectors at the quarter chord point of every column of vortex rings along the span. The force-moment pair is then transfered to the neighboring nodes using the same interpolation weighing procedure as in the linear case, while ensuring to maintain the equivalence of the force-moment pair. This viscous coupling extends the method to the transonic regime where the pitching moment differs from the inviscid prediction, as well as separated flows.

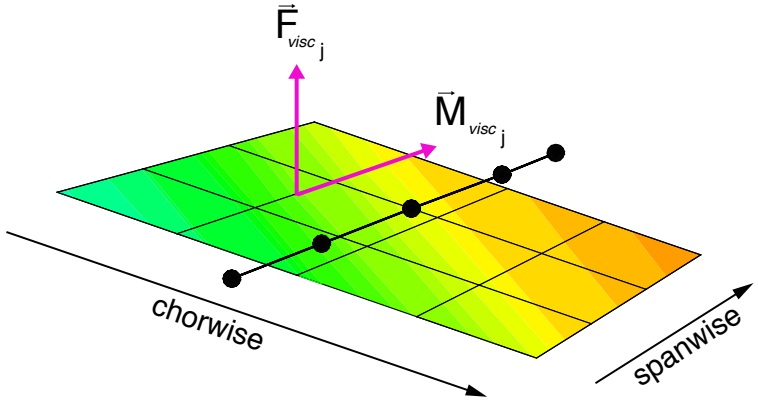

Figure 12: Viscous loads to be applied onto the FEM for each column of vortex rings

5 RESULTS

5.1 Trimming the HALE aircraft

To validate the static deflections produced by the segregated coupling algorithm, the HALE aircraft [1] is subjected to steady flight at $Vt = 25$m/s and its stiffness varied according to the stiffness parameter σ. The aircraft is then trimmed for angle of attack and elevator deflection by coupling the inviscid VLM with the FEM beam model and then solving for geometrically-nonlinear deflections.

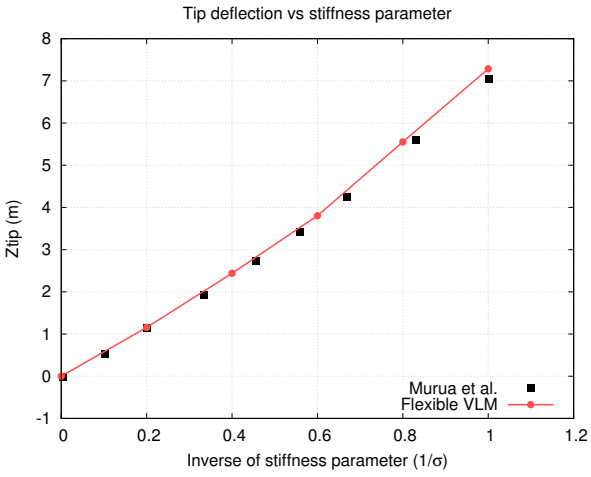

Figure 13: Trimmed tip deflection vs stiffness

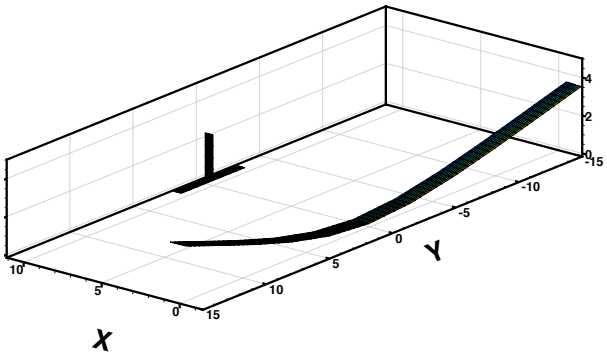

Figure 14: Deflections for $\sigma = 0.6$ and $\alpha = 7.5$deg

This has the benefit of simultaneously validating the inviscid aeroelastic coupling and the aircraft trimming procedure. The wing tip deflection is found to compare well with the results that were found by Murua et al[2012].

For every angle of attack that was studied, the aeroelastic coupling procedure has to converge to a potential energy and it can be observed in figure 15 that the potential energy of the structure and the work done by the aerodynamic converge towards a stable state under these conditions.

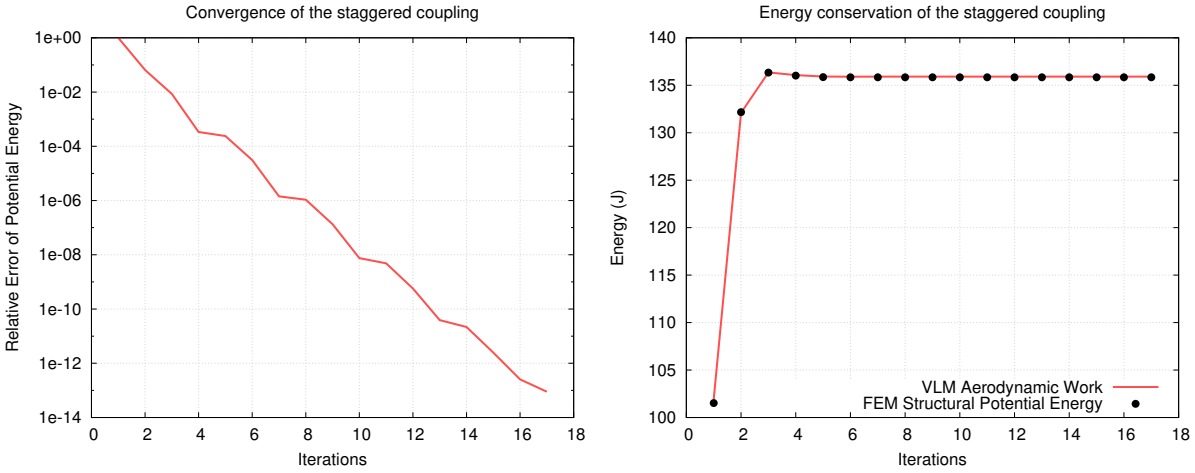

Figure 15: Convergence of the coupling (left) and energy conservation of the coupling (right) for $\sigma = 0.2$

5.2 CRM Wind Tunnel Correction

To validate the inclusion of the viscous coupling, a comparison of the C_L vs α curve for the wind tunnel model of the Common Research Model is presented [2]. It demonstrates that the deflection and twist experienced by the wing in the transonic flight regime reduce the overall lift that is generated for a given angle of attack.

It can be observed in figure 16, that the deviation of the lift coefficient provided by the NL-VLM is in good agreement with the more computationally expensive 3D CFD method used by Keye et al.[2014] for angles of attack lower than three degrees. We note the capability of the NL-VLM procedure to capture near-$C_{L_{max}}$ effects via the 2.5D CFD solutions. As anticipated, the $C_{L_{max}}$ is still heavily influenced by turbulence modeling [21], and several other factors, including transitional effects can account for the discrepancies observes in this region of the curve.

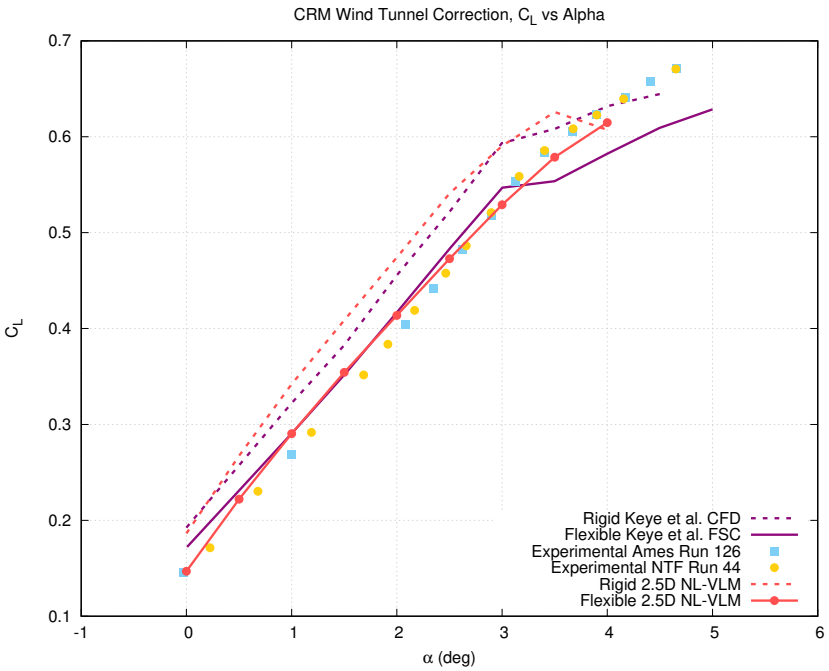

Figure 16: Lift coefficient vs angle of attack for the CRM-WT wing

At an angle of attack of 3.5 degrees, it can be observed that the rigid NL-VLM has attained its $C_{L_{max}}$, while the flexible NL-VLM hasn't yet, which suggests that the wing's flexibility has delayed the onset of stall to a higher angle of attack due to the negative twist that is incurred. This is corroborated by figures 18 and 19 where it can be observed that the flexibility of the wing causes significant washout. As a result, the wing loading is reduced and shifted inboard.

Figures 17 and 18 show good agreement with the higher fidelity methods used by Keye et al.[2014] for up to 80% of the span, whereas there is a significant discrepancy for the twist at the tip of the wing, which is indicative of differences with the wing loading experienced by the two methods near the wing tip. It is interesting to note that while both rigid methods experience a dip in C_L when nearing 3 degrees, the 2.5D NL-VLM does not experience any stall in the flexible case, which can be potentially explained by differences in turbulence modeling.

Figures 23 and 24 present the pressure distribution at three spanwise stations and compares

them with the results obtained by Keye et al.[2014], as well as experimental data. It can be observed that the difference in amplitude between rigid and flexible 2.5D NL-VLM is similar to the difference in amplitude observed by Keye et al.[2014]. However, the presence and position of the shock differs, a discrepancy that was observed by Gallay et al.[2017] for the CRM [5]. This is potentially due to the use of a constant sweep angle for the 2.5D solutions along the span (the quarter chord sweep in this case), whereas in reality the shock angle varies significantly along the span for the CRM wing. Furthermore, at span station $\eta = 0.727$, where the loading is roughly maximum according to figure 19 , the pressure distribution obtained by the present method is in good agreement with the experimental data.

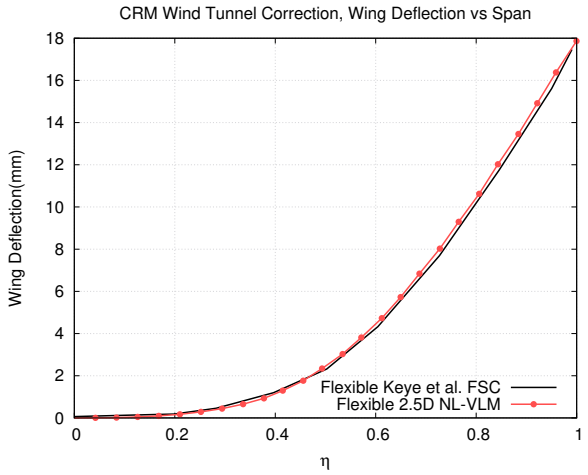

Figure 17: Deflections vs span for the CRM-WT wing at $\alpha = 3.0\ ^\circ$

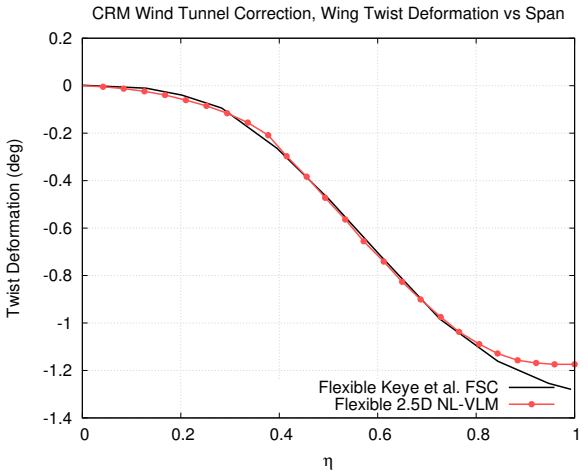

Figure 18: Twist deformation vs span for the CRM-WT wing at $\alpha = 3.0\ ^\circ$

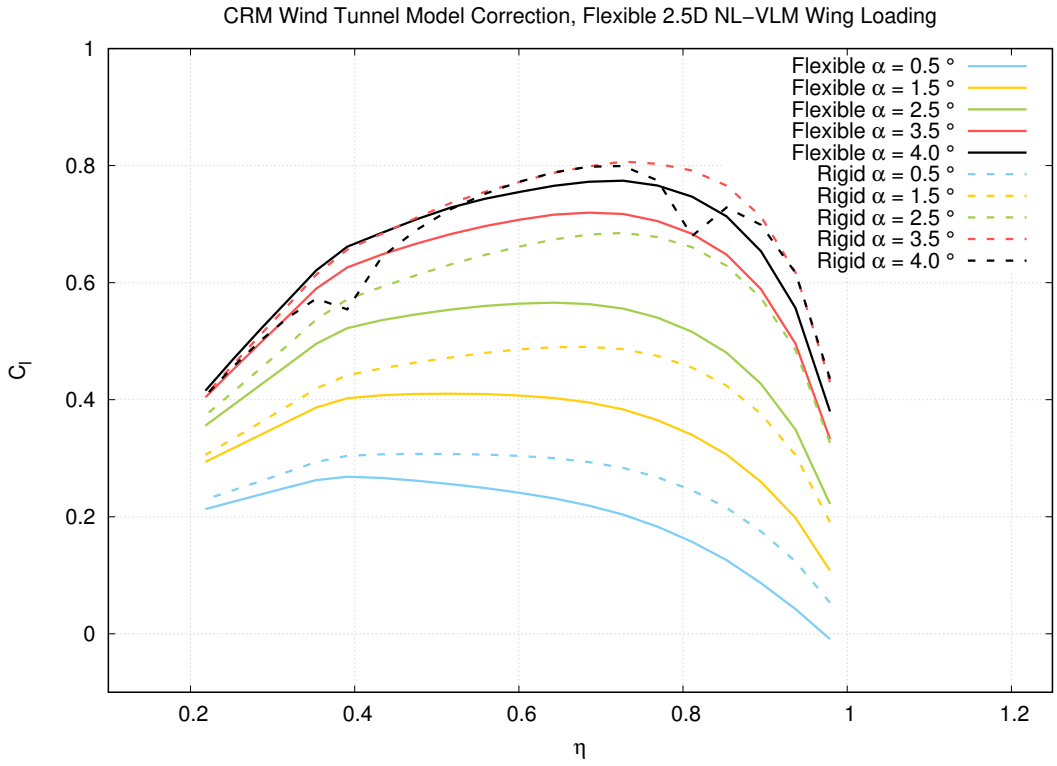

Figure 19: Wing loading vs angle of attack for the CRM-WT wing

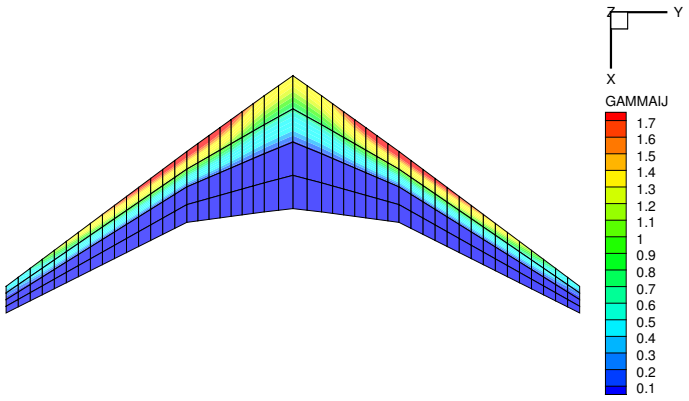

Figure 20: 44x4 VLM mesh for the CRM-WT wing overlayed with the γ distribution at $\alpha = 3.0\ ^{\circ}$

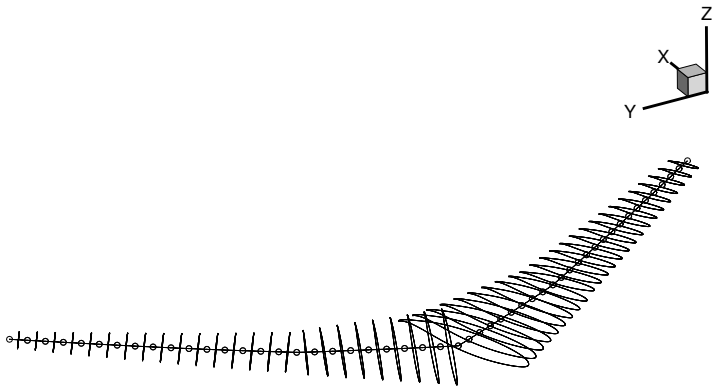

Figure 21: FEM model consisting of 50 beams with ‘ sections overlayed mid-beam

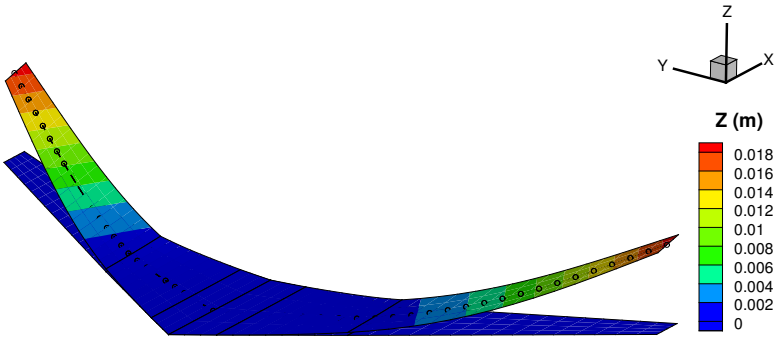

Figure 22: Deflections of the CRM-WT wing at $\alpha = 3.0\ ^{\circ}$, z-axis scaled 10x

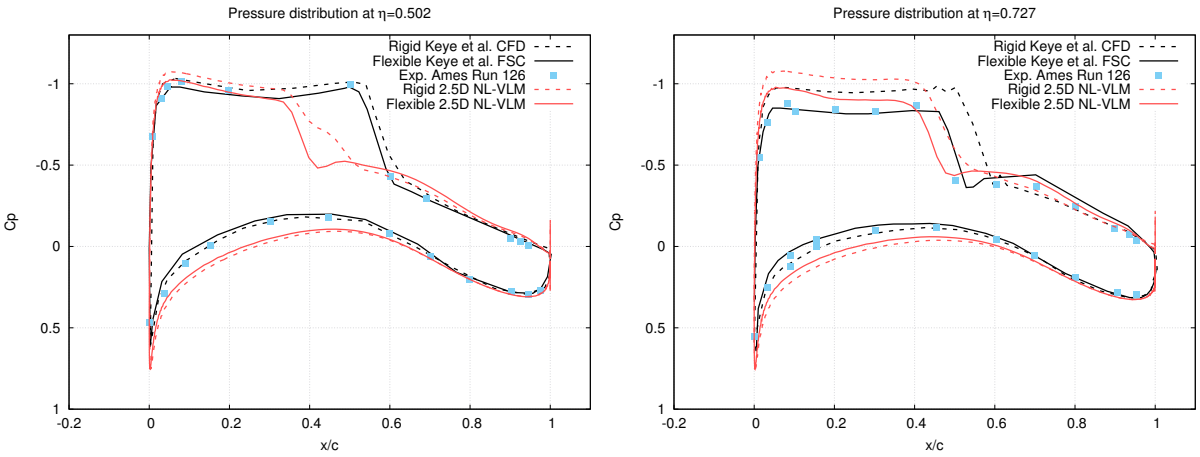

Figure 23: CRM-WT, Pressure distribution at $\eta = 0.502$ (left) and $\eta = 0.727$ (right) at $\alpha = 3.0$ °

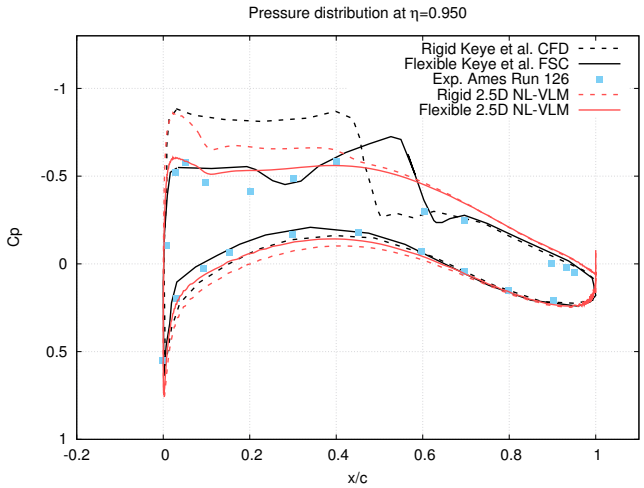

Figure 24: CRM-WT, Pressure distribution at $\eta = 0.950$ at $\alpha = 3.0$ °

5.3 Hirenasd Static Aeroelasticity

In the case of the Hirenasd wing, the pressure distributions obtained at an angle of attack of 1.5 degrees and a Mach number of 0.70 are compared in figures 28 through 34.

It can be observed that near the wing-fuselage junction, there is an important discrepancy between the flow predicted by the present method and the experimental data, which is to be expected for this method, since fuselage interference effects are neglected. However, as the span station increases, the agreement is seen to improve and offer a good approximation of the flow field for the purpose of aeroelastic deflection.

It should be noted that due to the high stiffness of the wing, the deflections are small and the magnitude of their impact on the pressure distribution is small.

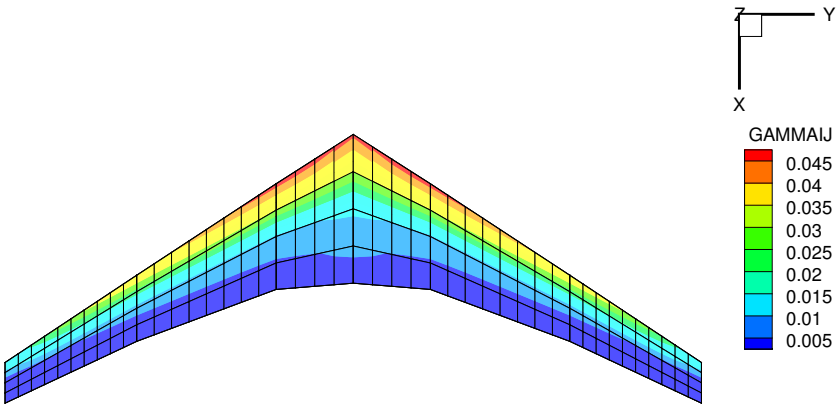

Figure 25: 44x4 VLM mesh for the HIRENASD wing overlayed with the γ distribution at $\alpha = 1.5$ °

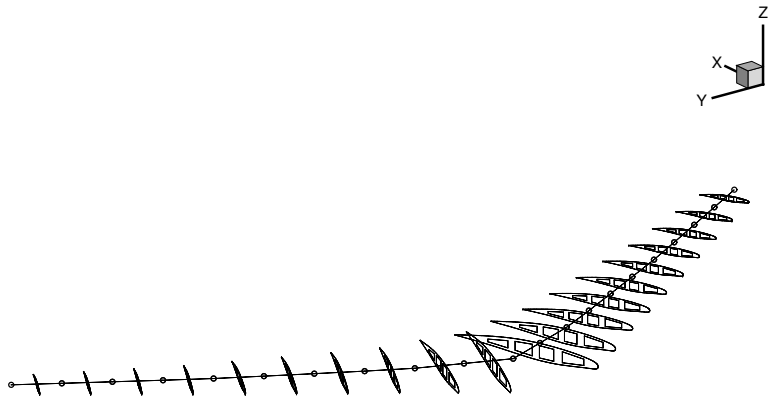

Figure 26: FEM model consisting of 20 beams for the HIRENASD wing with beam sections overlayed mid-beam

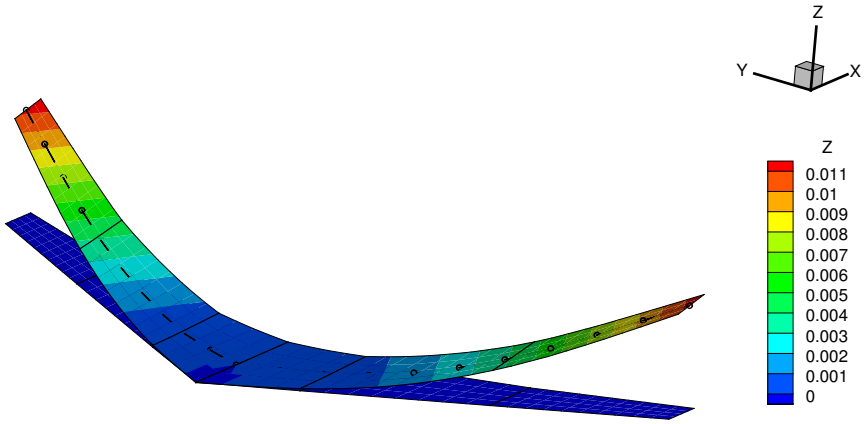

Figure 27: Deflections of the HIRENASD wing at $\alpha = 1.5$ °, z-axis scaled 33x

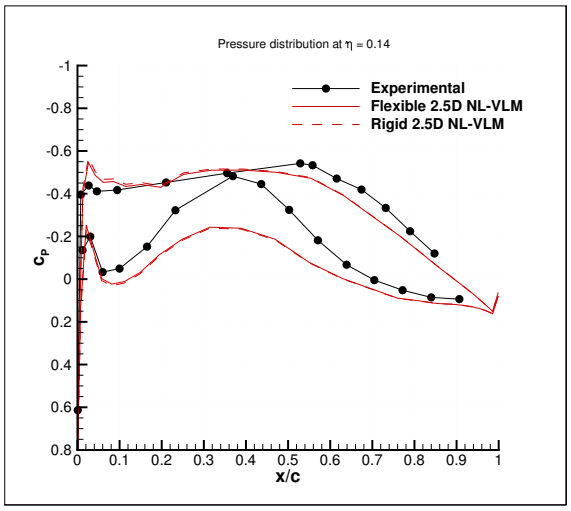

Figure 28: Hirenasd, Pressure distribution at $\eta = 0.14$

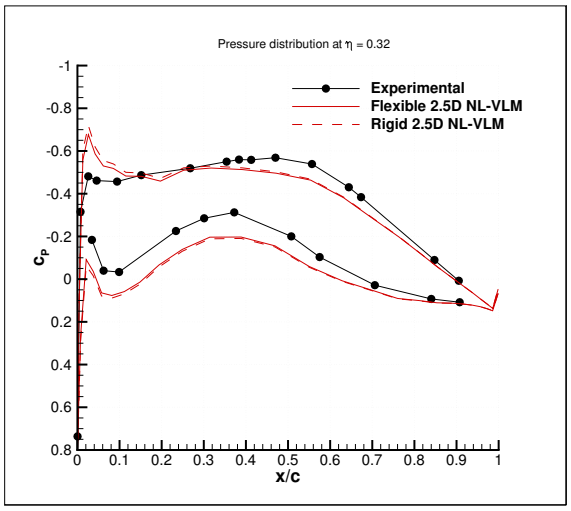

Figure 29: Hirenasd, Pressure distribution at $\eta = 0.32$

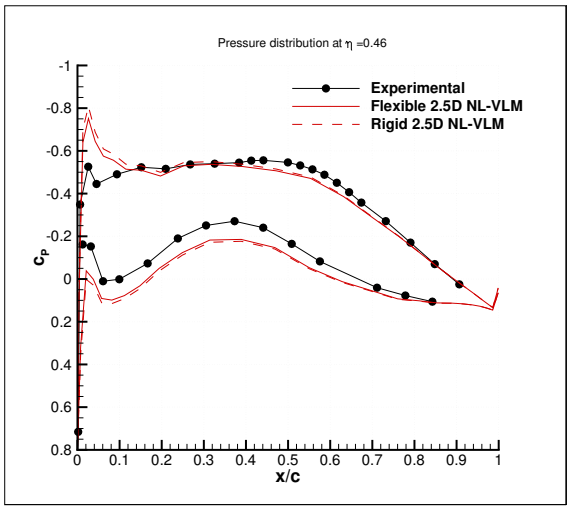

Figure 30: Hirenasd, Pressure distribution at $\eta = 0.46$

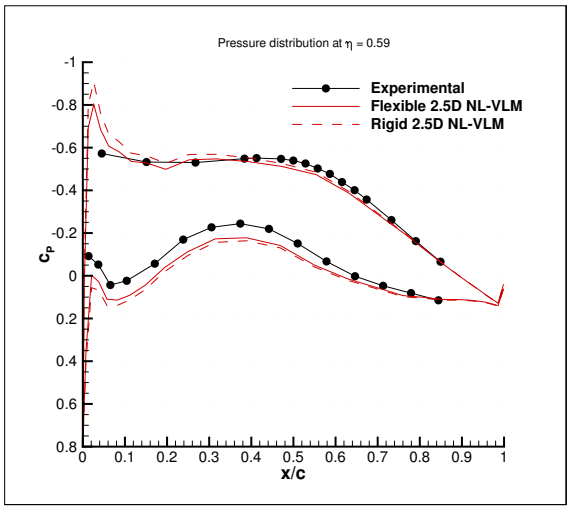

Figure 31: Hirenasd, Pressure distribution at $\eta = 0.59$

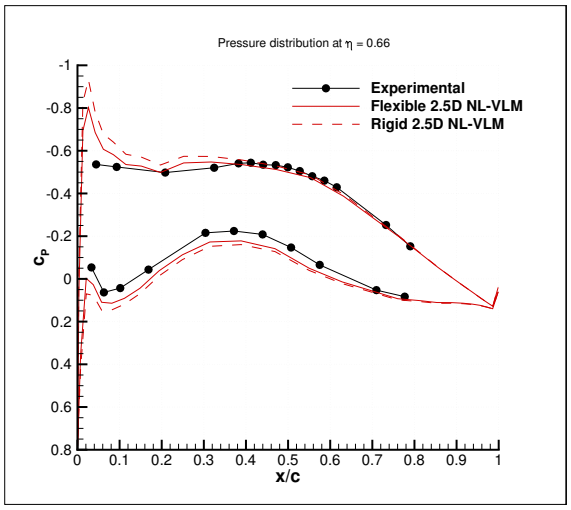

Figure 32: Hirenasd, Pressure distribution at $\eta = 0.66$

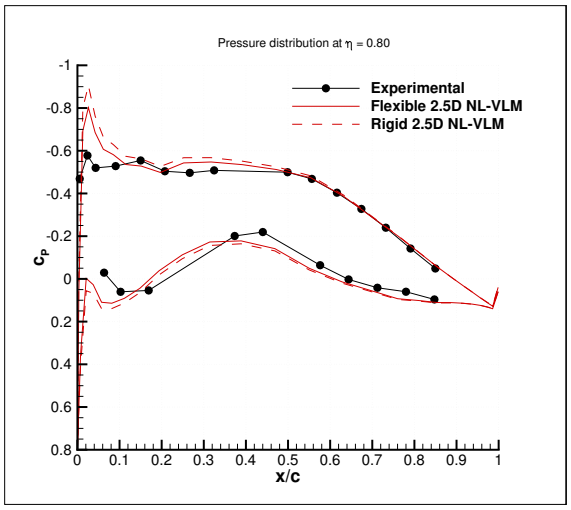

Figure 33: Hirenasd, Pressure distribution at $\eta = 0.80$

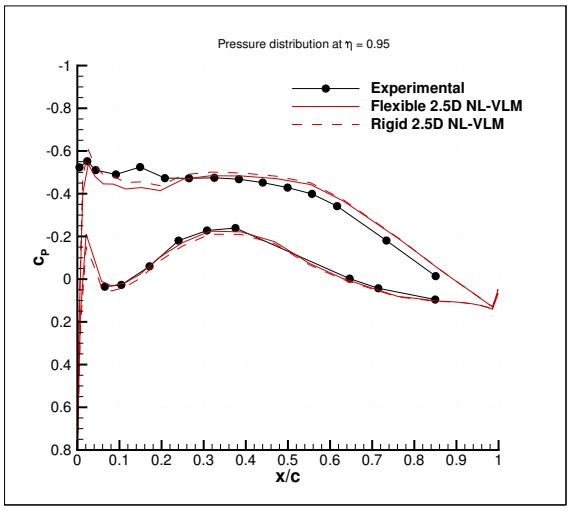

Figure 34: Hirenasd, Pressure distribution at $\eta = 0.95$

6 CONCLUDING REMARKS

A static aeroelastic formulation using the 2.5D Non-Linear Vortex-Lattice method was developed by coupling it with a finite-element beam model of similar computational cost and in a staggered fashion. This approach was verified on cases taken from the literature in both subsonic and transonic flight regimes. The results obtained demonstrate that the 2.5D NL-VLM method offers a medium-fidelity approximation of the three-dimensional flow and is capable of providing adequate pressure distributions for aeroelastic coupling. The computational cost of this method is significantly lower than high-fidelity methods and therefore offers potential with regards to aero-structural planform optimization.

7 ACKNOWLEDGMENT

The work has been performed through a Collaborative R&D Grant with Bombardier Aerospace, the Consortium de Recherche et d'innovation en Aerospatiale au Quebec (CRIAQ) and the Natural Sciences and Engineering Research Council of Canada (NSERC).

8 REFERENCES

[1] Murua, P. R., J. and Graham, M. (2012). Applications of the unsteady vortex-lattice method in aircraft aeroelasticity and flight dynamics. *Progress in Aerospace Sciences*, 46, 55–72.

[2] Keye, S. and Brodersen, O. (2014). Investigation of aeroelastic effects on the nasa common research model. *Journal of Aircraft*, 51(4), 1323–1330.

[3] Chwalowski, P. et al. (2011). Preliminary computational analysis of the hirenasd configuration in preparation for the aeroelastic prediction workshop. *International Forum on Aeroelasticity and Structural Dynamics*.

[4] Gallay, S. and Laurendeau, E. (2015). Non linear generalized lifting line coupling algorithms for pre/post stall flows. *AIAA Journal*, 53(7), 1784–1792.

[5] Gallay, S. and Laurendeau, E. (2016). Preliminary-design aerodynamic model for complex configurations using lifting-line coupling algorithm. *Journal of Aircraft*, 53(4), 1145–1159.

[6] Prananta, B. et al. (2012). Transonic unsteady aerodynamic analysis of hirenasd wing oscillating in flexible modes. *Contribution to AIAA Aeroelastic Workshop I*.

[7] Schuster, D. et al. (2013). Analysis of test case computations and experiments for the first aeroelastic prediction workshop. *51st AIAA Aerospace Sciences Meeting*.

[8] Piperni, D. A., P. and Henderson, R. (2013). Development of a multilevel multidisciplinary-optimization capability for an industrial environment. *AIAA Journal*, 51(10), 2335–2352.

[9] DeBlois, A. and Abdo, M. (2010). Multi-fidelity multidisciplinary design optimization of metallic and composite regional and business jets. *13th AIAA/ISSMO Multidisciplinary Analysis Optimization Conference*.

[10] Katz, J. and Plotkin, A. (1991). *Low-Speed Aerodynamics*. McGraw-Hill.

[11] Bourgault-Cote, S. et al. (2017). Extension of a two-dimensional navier-stokes solver for infinite swept flow. *AIAA Journal*, 55(2), 662–667.

[12] Hasanzadeh K., L. E. and Paraschivoiu, I. (2016). Grid-generation algorithms for complex glaze-ice shapes reynolds-averaged navierstokes simulations. *AIAA Journal*, 54(3), 847–860.

[13] Pigeon, L. A. T., A. and Laurendeau, E. (2014). Two-dimensional navierstokes flow solver developments at ecole polytechnique de montreal. *CFD Society of Canada 22nd Annual Conference*, 8.

[14] Levesque, A. T. (2015). Development of an overset structured 2d rans/ urans navierstokes solver using an implicit space and non-linear frequency domain time operators. *M.S. Thesis Polytechnique Montral*.

[15] Cook, M. D. P. M., R.D. and Witt, R. (2001). *Concepts and Applications of Finite Element Analysis*. John Wiley & Sons Inc.

[16] Wright, J. and Cooper, J. (2007). *Introduction to Aircraft Aeroelasticity and Loads*. London: Wiley & Sons.

[17] Singer, M. (1993). A general approach to moment calculation for polygons and line segments. *Pattern Recognition*, 26(7), 1019–1028.

[18] Farhat, L. M., C. and LeTallec, P. (1998). Load and motion transfer algorithms for fluid-structure interaction problems with non-matching discrete interfaces/ momentum and energy conservation, optimal discretization and application to aeroelasticity. *Computer methods in applied mechanics and engineering*, 157(1), 95–114.

[19] Farhat, C. and Lesoinne, M. (1998). Two efficient staggered algorithms for the serial and parallel solution of three-dimensional nonlinear transient aeroelastic problems. *Computer methods in applied mechanics and engineering*, 182(3), 499–515.

[20] de Boer, v. Z. A., A and Bijl, H. (2007). Review of coupling methods for non-matching meshes. *Computer methods in applied mechanics and engineering*, 196(8), 1515–1525.

[21] Rumsey, C. et al. (2011). Summary of the first aiaa cfd high-lift prediction workshop. *Journal of Aircraft*, 48(6), 2068–2082.

COPYRIGHT STATEMENT